

Efficient Photodegradation of Endocrine-Disrupting Chemicals with Bi₂O₃–ZnO Nanorods Under a Compact Fluorescent Lamp

Sze-Mun Lam · Jin-Chung Sin ·
Ahmad Zuhairi Abdullah ·
Abdul Rahman Mohamed

Received: 22 September 2012 / Accepted: 10 April 2013 / Published online: 28 April 2013
© Springer Science+Business Media Dordrecht 2013

Abstract Nanoscaled Bi₂O₃ particles coated on ZnO nanorods (ZNRs) have been fabricated by combining hydrothermal technique with a chemical precipitation method. X-ray diffraction, field emission-scanning electron microscopy, transmission electron microscopy, energy dispersive X-ray spectroscopy, Fourier transform infrared spectroscopy, and UV–vis absorption and photoluminescence studies were adapted to characterize the structure, morphologies, and optical properties of the nanocomposites. The results indicated that small Bi₂O₃ nanoparticles were well distributed on the surfaces of ZNRs. And the Bi₂O₃–ZNR nanocomposites showed high charge separation efficiency and •OH generation ability as evidenced by photoluminescence spectra. Under irradiation of a 55-W compact fluorescent lamp, the Bi₂O₃–ZNR nanocomposites demonstrated photocatalytic activities higher than pure ZNRs in the degradation of two endocrine-disrupting chemicals, phenol and methylparaben, which might be attributed to the high separation efficiency of photogenerated electron–hole pairs based on the cooperative role of Bi₂O₃ loading on ZNRs. Moreover, the Bi₂O₃–ZNR nanocomposite could be easily recovered and reused due to their one-dimensional nanostructural property. All these characteristics brought enormous benefits of Bi₂O₃–ZNR

nanocomposites to the practical application in indoor environmental remediation.

Keywords Zinc oxide · Bismuth oxide · Nanocomposite · Photocatalytic · Endocrine-disrupting chemical

1 Introduction

The environmental pollution of endocrine-disrupting chemicals (EDCs) in water sources and factory effluents has aroused great concern nowadays because they can exert hormonal imbalance activity and interfere with the functions of endocrine systems (Gultekin and Ince 2007; Walker 2009; Huang and Chen 2010; Sin et al. 2012). Numerous adverse effects including neuro-behavioral disorder, male and female infertility, sexual underdevelopment, birth defects, impaired immune function, and varieties of cancers are induced by EDCs. Some of the effects have been found in ecosystem and potentially take place in public health (Benotti et al. 2009; Brouwers et al. 2011), and thus, an effective environmental technology for the substantial removal of EDC from the body of water is required. Semiconductor-based photocatalysis has been shown to effectively remove EDCs within a short reaction period. Among the semiconductor photocatalyst available, zinc oxide (ZnO), with a high chemical stability and UV-sensitive property, has made photocatalysis as a promising option for sustainable and environment-

S.-M. Lam · J.-C. Sin · A. Z. Abdullah ·
A. R. Mohamed (✉)
School of Chemical Engineering, Universiti Sains Malaysia,
Engineering Campus,
14300 Nibong Tebal, Pulau Pinang, Malaysia
e-mail: chrahman@eng.usm.my

friendly treatments (Flores et al. 2011; Lam et al. 2012). Nevertheless, a major factor limiting the efficiency of ZnO photocatalytic processes is the quick electron–hole recombination which results in waste of energy supplied by the photon. Considerable efforts have been made to prevent the recombination of charge carriers in the semiconductor and improve the photocatalytic efficiency of ZnO, such as doping with transition metal ions, deposition of noble metals and coupling with other semiconductors such as CdS–ZnO, CeO₂–ZnO, ZnO–WO₃, and TiO₂–ZnO (Nayak et al. 2008; Lau et al. 2010; Pant et al. 2011; Lam et al. 2013a). In fact, coupling ZnO with narrow-band-gap semiconductors has been the subject of broad interest over the past few years as an approach to enhance the photocatalytic efficiency via promoting the electron and hole transfer and shifting the light absorption to visible range. It also proved that the efficient transfer of electron and hole from ZnO to reactants can lower the photocorrosion of ZnO to certain extent (Wang et al. 2010; Liu et al. 2011), so as to improve the stability of ZnO for long-term applications.

Morphologies and microstructures play an important role in the photocatalytic activity of ZnO. Many studies concerning the one-dimensional structures of ZnO such as nanowires, nanorods, nanotubes, and so on have been undertaken (Jia et al. 2009; Lam et al. 2013b; Sin et al. 2013). Recently, the preparation of ZnO nanorods has also attracted much attention because of their high surface-to-volume ratio and good dispersibility in solution (Wang et al. 2008; Mohajerani et al. 2009). Despite the fact that many papers have focused on the fabrication of nano- and microscale rods, most of these studies focused on the synthesis and morphology of pure phase ZnO. However, to the best of our knowledge, the reports on the synthesis of ZnO mixed metal–oxide systems with nanorod morphology are scarce up to now. In comparison to nanoparticles, ZnO nanorods can be widely used in many applications such as ultraviolet photodetectors, gas sensors, field-effect transistors, light-emitting device arrays, and photocatalysis for degradation and elimination of environmental pollutants (Park et al. 2006; Yang et al. 2012). Nanorods also have many merits compared to particles because of the enhancement of light absorption and rapid diffusion of reactive species transport along the long direction.

In this work, we report for the first time the synthesis of Bi₂O₃–ZnO nanorods (Bi₂O₃–ZNRs) via hydrothermal technique incorporating with a chemical-precipitation method. The Bi₂O₃ with narrow band gap of 2.8 eV was selected as the investigation material due to its wide potential applications in sensor technology, optical coatings, electrochromic materials, and gas- and liquid-phase pollution control (Hameed et al. 2009; Qiu et al. 2011). The prepared samples were characterized by different techniques and were used for the photodegradation of two EDCs, including phenol and methylparaben under irradiation by a compact fluorescent lamp. The utilization of a compact fluorescent lamp, which is a regularly used daily-living light source, could reduce additional energy consumption, and most of all, it could also be given an opportunity for practical applications in an indoor environment. Moreover, it provided a safer, more easily available, cheaper, and environment-friendly option for organic pollutant degradation.

2 Experiment

2.1 Synthesis Procedure

All the chemical reagents used in this work, including H₂O₂ (30 vol%), Bi(NO₃)₃·5H₂O, NH₄OH (25 wt% NH₃), and ethanol, were in analytical grade and purchased from Acros Organics. The detailed synthesis procedure for pure ZNRs was as follows: 2.0 g of ZnO powder was weighted into a Teflon-lined stainless steel autoclave of 200-mL capacity. Subsequently, 150 mL of 30 vol% H₂O₂ solution was added in with stirring. The autoclave was sealed and maintained at a temperature of 180 °C for 24 h and then allowed to cool to room temperature naturally. Bi₂O₃–ZNR nanocomposites were prepared by a chemical precipitation method. The typical procedure for the preparation of Bi₂O₃–ZNR nanocomposites was as follows: 1.0 g of ZnO nanorods was dispersed in 50 mL deionized water, and the suspension was ultrasonicated for 30 min. Then, a stoichiometric amount of Bi(NO₃)₃·5H₂O in 0.9 mL of NH₄OH was added to the ZnO suspension and stirred magnetically for 12 h. The as-formed precipitates were filtrated, washed with deionized water and ethanol and dried in air at 60 °C for 12 h. Finally, the prepared samples were calcined at 400 °C for 2 h with a heating rate of 2 °C/min.

2.2 Characterization

The obtained samples were characterized using an X-ray diffractometer (XRD; Philips PW1820) with Cu K α radiation. The morphology of the nanocrystallites was studied using a field emission-scanning electron microscope (FESEM; LEO SUPRA 50VP), and the microstructures were analyzed in-depth using a high-resolution transmission electron microscope (TEM) along with a high-resolution transmission electron microscope (HRTEM; Philips CM-12). The composition of Bi₂O₃ in ZnO nanorods was confirmed using energy dispersive X-ray spectroscopy (EDX). The infrared spectra were recorded in the range 4,000–500 cm⁻¹ on a Fourier transform infrared spectrometer (FTIR; Thermo scientific Nicolet IS10). The absorption spectra were obtained using a UV–vis spectrometer (Perkin Elmer Lambda 35) with BaSO₄ as reference. Photoluminescence (PL) measurement was performed using a spectrofluorometer (Perkin Elmer Lambda S55) using a Xe lamp with an excitation wavelength of 325 nm at room temperature.

2.3 Photocatalytic and Hydroxyl Radical (\bullet OH) Tests

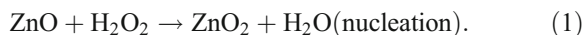
The photocatalytic activities of the as-prepared Bi₂O₃–ZNRs were evaluated by the degradation of EDC aqueous solution. The experiments were carried out as follows: 100 mg of the sample was dispersed in 100 mL of 2.1×10^{-4} M phenol solution in a 150-mL beaker. During all experiments, air was bubbled through the solution at a fixed flow rate of 6 mL/min using a specular draft tube. The suspension was continuously stirred with the aid of a magnetic stirrer. The heterogeneous mixture was equilibrated for 1 h in the dark. Subsequently, the solution was irradiated under a 55-W compact fluorescent lamp. The average light intensity striking the surface of the reaction solution was about 14,500 lux, as measured by a digital luxmeter. This lamp was fixed about 12 cm above the reaction solution. At specific time intervals, 2 mL of the sample was withdrawn from the system and centrifuged, and then, the concentration of the phenol at different time intervals was monitored by HPLC (Perkin Elmer Series 200). The HPLC system was reported in our previous studies (Lam et al. 2010). The HPLC analysis condition for phenol was detector wavelength of 254 nm and water-/acetonitrile ($\varphi_r=7 : 3$) mobile phase mixture (or detector wavelength of

254 nm and water-/methanol ($\varphi_r=5 : 5$) mobile phase mixture for methylparaben). By the same methods, the photocatalytic degradation efficiencies of methylparaben in the presence of prepared samples could be measured. \bullet OH analysis was conducted using experimental procedures as follows: 100 mg of the sample was dispersed in 20 mL of the 5×10^{-4} M terephthalic acid (TA) aqueous solution with a concentration of 2×10^{-3} M NaOH at room temperature. The same condition was applied to irradiate the above suspension as for the photocatalytic activity evaluation of catalysts. After 180-min irradiation of fluorescent light, 5 mL of the sample was withdrawn from the system, centrifuged, and then monitored using spectrofluorometer (Perkin Elmer Lambda S55) to measure the PL intensity at 425 nm induced with 315-nm excitation. In order to determine the reproducibility of the results, at least duplicated runs were carried out for each condition for averaging the results, and the experimental error was found to be within ± 4 %.

3 Results and Discussion

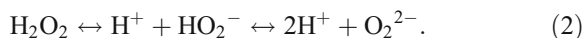
3.1 Mechanism of Nanorod Formation

ZnO is a polar crystal showing positive and negative polar planes, rich in Zn and O [Liu et al. 2007; Zhang et al. 2008]. Typically, it was believed that the morphology of ZnO crystals was related to both their intrinsic crystal structure and their external factors (Zhang et al. 2002, 2004). The possible mechanisms for the formation of single crystalline ZnO nanorod-like structures could be understood from the mechanism scheme given below.



In hydrothermal synthesis, the starting materials used were only ZnO powder and 30 vol% H₂O₂ aqueous solution, and ZnO₂ was the sole resulting solid. Thus, it was believed that ZnO₂ may be formed as shown in Eq. 1. Since no valence change of Zn and O occurred, the formation of ZnO₂ was just through a precipitation conversion reaction (Liu et al. 2012). That is, ZnO powder increasingly dissolved in the H₂O₂ aqueous solution under the relatively high-temperature and high-pressure hydrothermal environment, giving rise to Zn²⁺ ions. On the other hand, a

part of H_2O_2 would dissociate in water to form peroxide anions (O_2^{2-}) according to Eq. 2.



When the concentration of Zn^{2+} and O_2^{2-} reached the saturation level, ZnO_2 nuclei were formed. It was considered that the as-prepared ZnO_2 nuclei may serve as building blocks for the formation of a single crystal growth of ZnO_2 . With reaction time under proper heating conditions, the ZnO_2 nuclei concentration increased, which led to the growth of ZnO_2 nanocrystals into nanorod-like structures. Nevertheless, the as-prepared ZnO_2 nanorods were thermally unstable and would thoroughly decompose into ZnO and O_2 when heated in air at 400°C for 2 h as in Eq. 3.



3.2 Characterization

Figure 1 presents the XRD patterns of the pure ZNRs and the Bi_2O_3 -ZNR nanocomposites with different loadings of Bi_2O_3 . Figure 1(e) shows that the crystal phase of the ZNRs agreed with wurtzite structure (JCPDS file No. 36-1451). From Fig. 1(b–d), all of the peaks can be indexed to the monoclinic phase of α - Bi_2O_3 except the diffraction peaks of ZnO , which was well matched with the standard from JCPDS file No. 41-1449. No other crystalline impurities were

detected, demonstrating the phase purity of the products. Compared to bulk Bi_2O_3 in Fig. 1(a), the broadening of these peaks that belong to Bi_2O_3 suggested the presence of small bismuth oxide particles (Qiu et al. 2011). As estimated from the half-peak width using the Scherrer's equation, the average crystal sizes of Bi_2O_3 were about 21.5, 34.3, and 59.7 nm accordingly for Bi_2O_3 (0.5 at.%)–ZNRs, Bi_2O_3 (1 at.%)–ZNRs, and Bi_2O_3 (2 at.%)–ZNRs, respectively. The XRD patterns can illustrate that the as-synthesized samples were comprised of two-phase structure of wurtzite ZnO and monoclinic phase Bi_2O_3 . Moreover, the XRD peaks belonging to ZnO in the Bi_2O_3 -ZNR nanocomposites do not shift compared with the pure ZNRs, which can be implied that the Bi does not substitute into the ZnO lattices for the Zn.

Figure 2a, b depicts the typical FESEM images of the pure ZNRs and Bi_2O_3 (1 at.%)–ZNR nanocomposites. As shown in Fig. 2a, the pure ZNRs composed of a number of non-uniform nanorod-like structures with average diameters of about 79.5 nm. Figure 2b shows the nanorods of coupled semiconductors along with some spherical shape nanoparticles, and the average diameter of the rods was 55.1 nm. The average diameters of the pure ZNRs were larger than the Bi_2O_3 (1 at.%)–ZNR nanocomposites. The result of EDX analysis in the inset of Fig. 2b implied that the nanocomposites contained Zn, O, and a small amount of Bi elements. The content of bismuth was analyzed to be

Fig. 1 X-ray diffraction patterns of *a* Bi_2O_3 , *b* Bi_2O_3 (0.5 at.%)–ZNRs, *c* Bi_2O_3 (1 at.%)–ZNRs, *d* Bi_2O_3 (2 at.%)–ZNRs, and *e* pure ZNRs

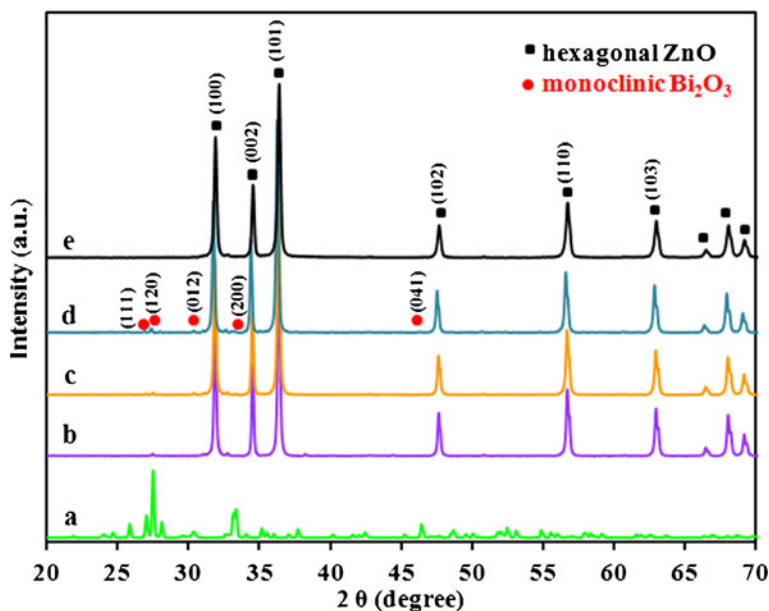
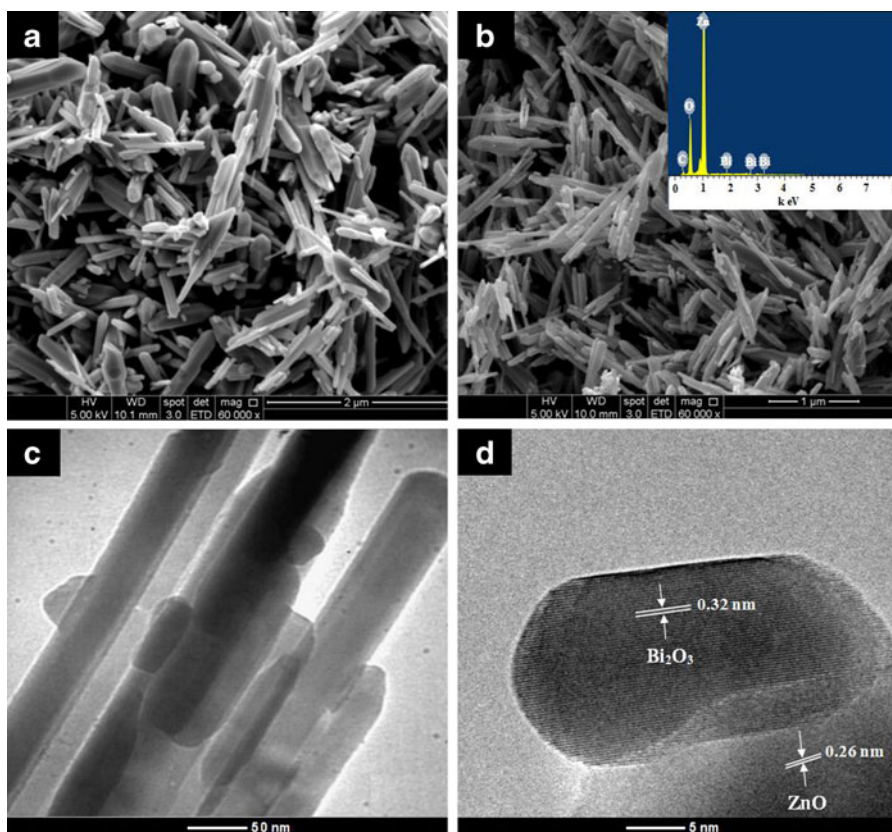


Fig. 2 **a** FESEM images of pure ZNRs, **b** FESEM images of Bi_2O_3 (1 at.%)–ZNR, **c** TEM image of Bi_2O_3 (1 at.%)–ZNR nanocomposites, and **d** HRTEM images of Bi_2O_3 (1 at.%)–ZNR nanocomposites. The *inset* of **b** shows the EDX spectrum of the Bi_2O_3 (1 at.%)–ZNR nanocomposites



0.91 at.%, which was closed to the experimental bismuth concentration. For detailed microstructure characteristics of the Bi_2O_3 –ZNR nanocomposites, TEM along with HRTEM analyses was done, and the results are indicated in Fig. 2c, d. Figure 2c displays the typical TEM image of Bi_2O_3 (1 at.%)–ZNRs. It can be clearly demonstrated that the Bi_2O_3 particles with the range of 25–36 nm were attached on the surface of ZNR matrix, which also coincided with the obtained XRD investigations. Moreover, the Bi_2O_3 nanoparticles cannot be separated from each other even by continuous ultrasonic dispersion in ethanol for 20 min before TEM analysis. Figure 2d shows that the HRTEM image of the interplanar distance of 0.32 nm was in accordance with the (120) crystal fringe of monoclinic phase Bi_2O_3 . In the case of the ZNRs, the space between the adjacent lattice fringes was 0.26 nm, corresponding to the interplanar distance of the (002) crystal fringes of wurtzite phase ZnO crystals. From the TEM and HRTEM images, it can be verified that the Bi_2O_3 –ZNR nanocomposites have highly crystalline structure, which was crucial for excellent photocatalytic materials.

FTIR spectra were also carried out to study the pure ZNRs and Bi_2O_3 –ZNR nanocomposites. In Fig. 3, the broad absorption band at $3,428\text{ cm}^{-1}$ corresponded to the –OH stretching vibrations of H_2O , and the band at $1,645\text{ cm}^{-1}$ can be associated with the bending vibrations of H_2O molecules present in all the prepared

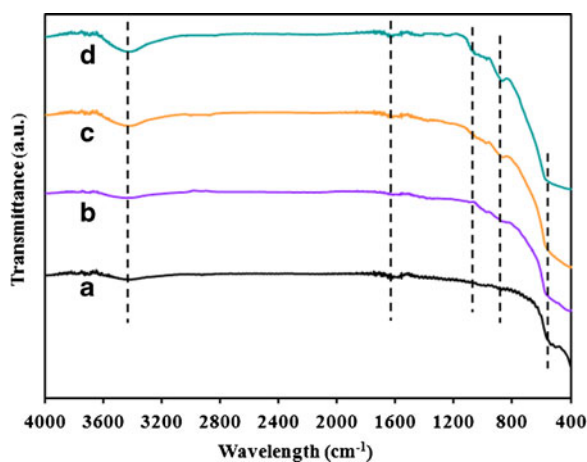


Fig. 3 FTIR spectra for samples *a* ZNRs, *b* Bi_2O_3 (0.5 at.%)–ZNRs, *c* Bi_2O_3 (1 at.%)–ZNRs, and *d* Bi_2O_3 (2 at.%)–ZNRs

samples. The pure ZNR spectrum (Fig. 3(a)) was dominated by the band at 542 cm^{-1} , which can be ascribed to the stretching of Zn–O bond. Apart from distinctive band of the Zn–O stretching bond, from Fig. 3(b–d), the FTIR spectra of the coupling nanocomposite displayed dominant bands for Bi_2O_3 nanoparticles. Concretely, the bands in the region $400\text{ to }600\text{ cm}^{-1}$ can be assigned to overlapping stretching vibrations of Bi–O bonds of BiO_6 coordination octahedra with the stretching of Zn–O bonds (Zhang et al. 2006; Kundu et al. 2009). Moreover, the weak to medium bands at 854 and $1,060\text{ cm}^{-1}$ can be observed with increasing Bi_2O_3 loading in the nanocomposites. These absorption bands were attributed to the other kinds of vibrations of Bi–O caused by the interaction between the Bi–O bonds and their other surroundings (Wang et al. 2009a). Furthermore, as for ZnO bands, the characteristic bands at $3,428\text{ cm}^{-1}$ became stronger with increasing Bi_2O_3 loading in the nanocomposite, inferring with the larger surface –OH group density on the catalyst. The –OH groups play a crucial role on the photocatalytic reaction since the photocatalytic process mainly occurs on the catalyst surface.

UV–visible absorption spectra of the Bi_2O_3 –ZNR nanocomposites along with the pure ZNRs were shown in Fig. 4. The absorption edge at a wavelength of about $380\text{--}400\text{ nm}$ for the pure ZNRs and Bi_2O_3 –ZNR nanocomposite samples can be seen. Comparing with pure ZNRs (Fig. 4(a)), additional broad tails from about 400 to 600 nm appeared in the spectra of the Bi_2O_3 –ZNR nanocomposites (as recorded in Fig. 4(b–d)). The result indicated that the absorption of Bi_2O_3 –ZNR

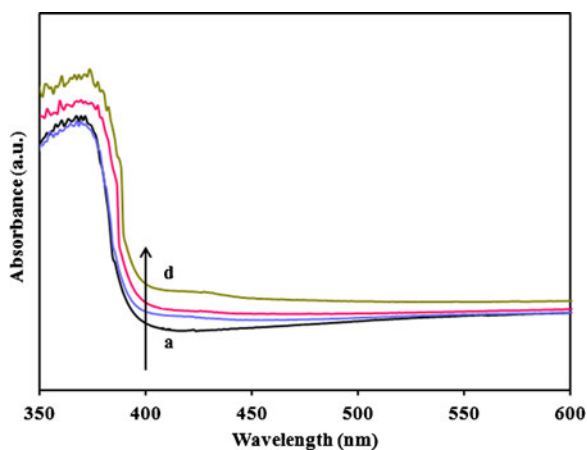


Fig. 4 UV–vis absorption spectra of *a* ZNRs and Bi_2O_3 –ZNR nanocomposites with different Bi_2O_3 loadings of *b* 0.5, *c* 1, and *d* 2 at.%

nanocomposites was enlarged to the visible spectrum due to the existence of Bi_2O_3 that modified the optical absorption edge. By increasing the loading of Bi_2O_3 in Bi_2O_3 –ZNRs, the absorption intensities of nanocomposites were enhanced. The band gap energies were calculated according to Eq. 4 (He et al. 2011):

$$E_g = hc/\lambda = 1243.1/\lambda, \quad (4)$$

where E_g is the band gap energy (eV), h is the Planck's constant (4.135667×10^{-15} eVs), c is the velocity of light (3×10^8 m/s), and λ is the wavelength (nm) of absorption onset. Using Eq. 4, the band gap energies of Bi_2O_3 (0.5 at.%)–ZNRs, Bi_2O_3 (1 at.%)–ZNRs, and Bi_2O_3 (2 at.%)–ZNRs were calculated as 3.19, 3.16, and 3.22 eV, respectively, lower than that of pure ZNRs (3.24 eV). In addition, all the Bi_2O_3 –ZNR nanocomposite absorption edge also showed a slight redshift. This result might be ascribed to the increase of particle size of Bi_2O_3 nanoparticles. The above results revealed that the Bi_2O_3 –ZNR nanocomposites can absorb in both UV and visible regions of the solar light. Hence, the absorption property deduced that the Bi_2O_3 –ZNR nanocomposites could be promising in visible-light photocatalysis compared with that of pure ZNRs.

3.3 Photocatalytic Activities

To evaluate the photocatalytic activity of as-synthesized Bi_2O_3 –ZNR nanocomposites, the degradation of phenol was carried out as a test reaction. Phenol was selected as a model pollutant since it is a common EDC in industrial wastewater and has good resistance to light degradation compared with other organic dyes (rhodamine B, methylene blue, etc.). More importantly, phenol cannot be photodegraded in the absence of any photocatalyst under visible-light irradiation. The HPLC profiles of phenol aqueous solution in the presence of Bi_2O_3 (1 at.%)–ZNR nanocomposites under irradiation by a 55-W compact fluorescent lamp at various durations are shown in Fig. 5a. The phenol showed a characteristic peak at a retention time (RT) of 5.6 min; it became weaker with the extended irradiation time and nearly disappeared after 360 min. In addition to the above-mentioned main compound, muconic acid at RT 1.1 min, pyrogallol at RT 1.6 min, hydroquinone at RT 2.2 min, resorcinol at RT 2.6 min, and benzoquinone at RT 3.3 min were the degradation intermediates when compared with the standard chemicals. This identification was also

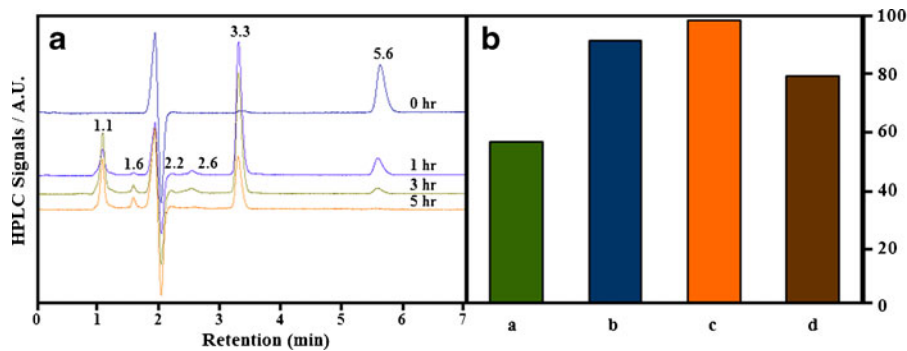


Fig. 5 **a** HPLC profiles of phenol solution with Bi_2O_3 (1 at.%)–ZNRs at different time intervals and **b** kinetics of photodegradation of phenol with **a** ZNRs and Bi_2O_3 –ZNR nanocomposites with

different Bi_2O_3 loadings of **b** 0.5, **c** 1, and **d** 2 at.% under a 55-W compact fluorescent lamp (dose of catalyst, 100 mg; concentration of phenol, 2.1×10^{-4} M; volume of phenol, 100 mL)

consistent with that reported in other studies (Sobczynski et al. 2004; Pardeshi and Patil 2008). As shown in Fig. 5b, the degradation efficiencies of phenol were about 56.4, 91.3, 98.5, and 79.2 % for the pure ZNRs, Bi_2O_3 (0.5 at.%)–ZNRs, Bi_2O_3 (1 at.%)–ZNRs, and Bi_2O_3 (2 at.%)–ZNRs, respectively, in 360 min. Obviously, all of the Bi_2O_3 –ZNR nanocomposite samples exhibited the enhanced photocatalytic activities in comparison with the pure ZNRs, while Bi_2O_3 (1 at.%)–ZNR nanocomposites displayed the best performance on the photodegradation activities among the four samples.

To further investigate the photocatalytic properties of the as-prepared photocatalyst, methylparaben was chosen to evaluate the photocatalytic activity as it was more difficult to be degraded than the phenols in aqueous media. Like phenol, methylparaben is a common EDC in industrial wastewaters, especially in personal care chemicals and pharmaceuticals, and studies have proven that it showed a certain estrogenic

activity even at trace levels (Harvey and Everett 2004; Pugazhendhi et al. 2005). Figure 6a shows the HPLC profiles of methylparaben aqueous solution at various durations in the presence of Bi_2O_3 (1 at.%)–ZNR nanocomposites. The methylparaben showed a characteristic peak at retention time (RT) 4.70 min; it gradually decreased during irradiation in 360 min. In addition to the above-mentioned main compound, 4-hydroxybenzoic acid at RT 1.3 min and hydroquinone at RT 2.1 min were the degradation intermediates when compared with the standard chemicals. As shown in Fig. 6b, the degradation efficiencies of methylparaben were about 38.1, 65.1, 72.6, and 54.3 % for the pure ZNRs, Bi_2O_3 (0.5 at.%)–ZNRs, Bi_2O_3 (1 at.%)–ZNRs, and Bi_2O_3 (2 at.%)–ZNRs, respectively, after 360 min. Similarly, all the Bi_2O_3 –ZNR nanocomposites showed the enhanced photocatalytic activities in comparison with the pure ZNRs, while Bi_2O_3 (1 at.%)–ZNR nanocomposites displayed

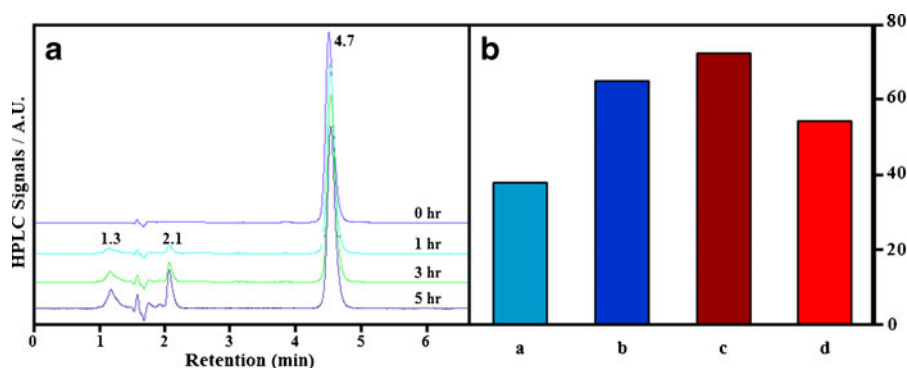


Fig. 6 **a** HPLC profiles of methylparaben solution with Bi_2O_3 (1 at.%)–ZNRs at different time intervals and **b** kinetics of photodegradation of methylparaben with **a** ZNRs and Bi_2O_3 –ZNR nanocomposites with different Bi_2O_3 loadings of **b** 0.5, **c**

1, and **d** 2 at.% under a 55-W compact fluorescent lamp (dose of catalyst, 100 mg; concentration of methylparaben, 1.3×10^{-4} M; volume of methylparaben, 100 mL)

the best performance on the photodegradation activities among the four samples.

Moreover, reusability as well as maintaining high photocatalytic activity of catalyst was an important issue for long-term use in practical applications. Thus, the stability of the catalyst to maintain its high activity over time needed to be considered. It was known that the photocorrosion or photodissolution of catalyst might occur on the photocatalyst surface in the photocatalytic reaction. To test the stability of $\text{Bi}_2\text{O}_3(1 \text{ at.}\%)\text{-ZNR}$ nanocomposites, the catalysts were reused three times by simple filtration and washing after reaction. As shown in Fig. 7, there were still considerable photocatalytic activities of the $\text{Bi}_2\text{O}_3(1 \text{ at.}\%)\text{-ZNR}$ nanocomposites in the recycling reactions. In fact, the $\text{Bi}_2\text{O}_3\text{-ZNR}$ nanocomposites have the merit of good sedimentation ability which was beneficial for recovery. The sedimentation ability of the as-synthesized $\text{Bi}_2\text{O}_3\text{-ZNRs}$ was investigated in the inset of Fig. 7a. After natural sedimentation for 30 min, the $\text{Bi}_2\text{O}_3\text{-ZNR}$ nanocomposites were rapidly settled at test bottle, probably due to the large length-to-diameter ratio of the one-dimensional structure. Hence, the $\text{Bi}_2\text{O}_3\text{-ZNR}$ nanocomposites not only showed enhanced photoactivity for the degradation of EDCs but also could easily recover from the reaction system.

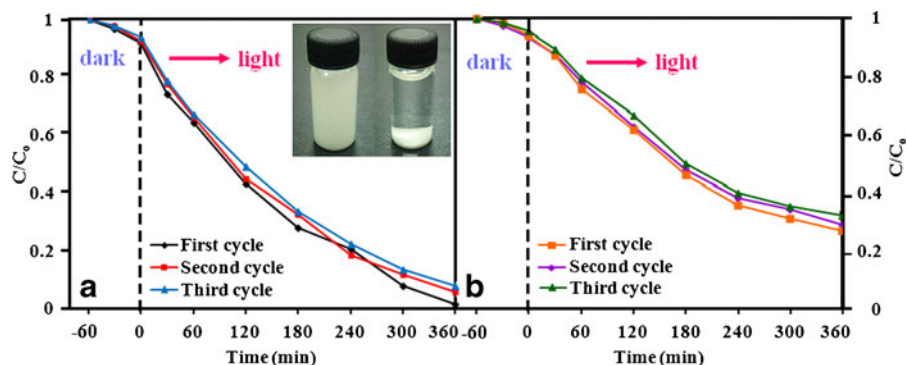
3.4 Photocatalytic Mechanism

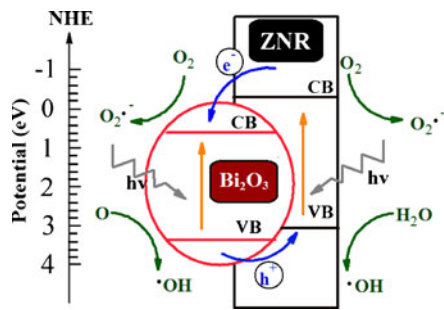
In general, the enhanced photocatalytic activity of $\text{Bi}_2\text{O}_3\text{-ZNR}$ nanocomposites can be explained by the improvement in charge transmission between the semiconductors ZnO (wide band gap) and Bi_2O_3 (narrow band gap) which prolonged the charge carriers' lifetime. Moreover, the photocatalytic performance of the coupled semiconductors was also related to the surface contact between particles, geometry of the particles, and

particle size. When the proportion of Bi_2O_3 was low (0.5 at.%), the effect of charge separation induced by Bi_2O_3 was not obvious because of the insufficiency of Bi_2O_3 . However, when the concentration of Bi_2O_3 increased to 2.0 at.%, higher surface coverage of Bi_2O_3 nanoparticles decreased the surface contact between the ZnO nanorods, which was not sufficient for the production of active radicals so as to reduce the photocatalytic activity (Wang et al. 2009b). On the other hand, it was considered to be a consequence of charge carrier dissipations by trapping when the loading amount of Bi_2O_3 came up to a certain level. The above statements implied that the photocatalytic activity was also governed by Bi_2O_3 content loaded on ZnO. In other words, there was a critical loading of Bi_2O_3 on ZnO for photocatalytic efficiency. The as-synthesized $\text{Bi}_2\text{O}_3(1.0 \text{ at.}\%)\text{-ZNR}$ nanocomposites with well dispersion and critical loading of Bi_2O_3 on the surface of ZnO exhibited higher photodegradation efficiencies for both EDCs as compared to that of other samples. Therefore, $\text{Bi}_2\text{O}_3(1.0 \text{ at.}\%)\text{-ZNR}$ nanocomposites were expected to be an optimum photocatalyst.

As for photocatalytic mechanism, a postulated mechanism for the enhanced photocatalysis of the $\text{Bi}_2\text{O}_3\text{-ZNR}$ nanocomposites under fluorescent light irradiation was elucidated in this paper. Consulting to the literature (Kaneko and Okura 2002), thermodynamic conditions such as the position of semiconductor conduction and valence bands of composite semiconductors favor the occurrence of the phenomenon of efficient interparticle charge transfer between the semiconductors ZnO and Bi_2O_3 . When ZnO (wide band gap) and Bi_2O_3 (narrow band gap) formed a coupled photocatalyst, Bi_2O_3 can be excited by photons under visible-light irradiation, and ZNRs may remain unexcited. Upon fluorescent-light excitation, an electron from the ZNR and Bi_2O_3 would be

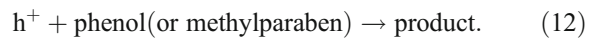
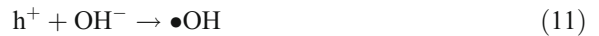
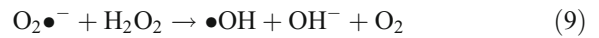
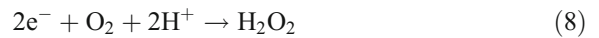
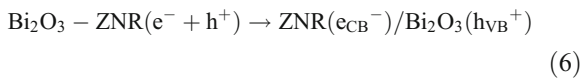
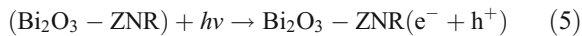
Fig. 7 Cyclic degradation curve for the $\text{Bi}_2\text{O}_3(1 \text{ at.}\%)\text{-ZNRs}$ under fluorescent light irradiation using 20 mg/L of **a** phenol and **b** methylparaben. The inset figure (**a**) shows the $\text{Bi}_2\text{O}_3(1 \text{ at.}\%)\text{-ZNRs}$ suspended in water (*left*) and settled naturally after 30 min (*right*)





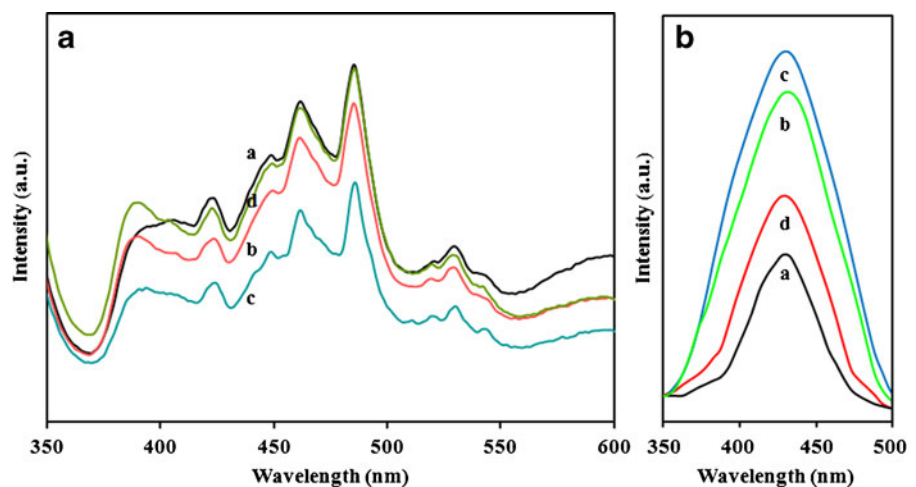
Scheme 1 The electron–hole separation and energy band structure of Bi₂O₃–ZNR nanocomposites under fluorescent light irradiation

promoted from the valence band to the conduction band, leaving behind a hole in the valence band. As the conduction band of Bi₂O₃ was lower than that of ZNR, the former can be used as a photoelectronic receiver. The photogenerated electrons of the ZNR conduction band will be migrated to the conduction band of Bi₂O₃. Since the holes move in the opposite direction from the electrons, photogenerated holes will be captured within the ZNR, making charge separation to become more effective. Scheme 1 shows an illustration of interparticle electron and hole transfer behavior. The mechanism for the photocatalytic degradation of phenol and methylparaben in these experiments was postulated as follows:



Furthermore, the enhanced photocatalytic mechanism can be characterized by PL spectroscopy, as the PL studies have been commonly used to evaluate the efficiency of charge carrier trapping, migration, and transfer and to provide insight into the fate of electron–hole pairs in semiconductors (He et al. 2011). Figure 8a depicts the PL spectra of pure ZNRs and Bi₂O₃–ZNR nanocomposites. The PL spectra patterns of all the samples of Bi₂O₃–ZNR nanocomposites indicated the dramatic decrease in emission yield as compared to pure ZNRs. Such a decrease in emission might be attributed to the efficient charge injection process between the Bi₂O₃ nanoparticles and ZNRs. In addition, the PL intensity of Bi₂O₃–ZNR nanocomposites changed with the altering of Bi₂O₃ amount. As for Bi₂O₃(1 at.%)–ZNR nanocomposites, the PL spectrum as shown in Fig. 8a was the lowest. Since the PL signal was the result of the recombination of charge carriers, the lower PL intensity

Fig. 8 a Photoluminescence spectra and **b** •OH generation ability analysis of *a* ZNRs, *b* Bi₂O₃(0.5 at.%)–ZNRs, *c* Bi₂O₃(1 at.%)–ZNRs, and *d* Bi₂O₃(2 at.%)–ZNRs



showed a lower recombination rate of charge carriers (Jia et al. 2009). It inferred that $\text{Bi}_2\text{O}_3(1 \text{ at.}\%)\text{-ZNR}$ nanocomposites have the lowest electron and hole recombination rate, suggesting that the electrons and holes have longer lifetime and may generate larger amount of active $\bullet\text{OH}$.

The $\bullet\text{OH}$ radical formations on the surface of $\text{Bi}_2\text{O}_3\text{-ZNR}$ nanocomposites irradiated by fluorescent light were detected by PL technique with terephthalic acid (TA) as a probe molecule in this study. It can be seen that the PL intensities were enhanced to maximum $\text{Bi}_2\text{O}_3(1 \text{ at.}\%)\text{-ZNRs}$ and then decreased with increasing Bi_2O_3 loading (Fig. 8b). This indicated that the fluorescence was caused by chemical reactions of TA with $\bullet\text{OH}$ formed in photocatalytic reactions (Ishibashi et al. 2000; Wang et al. 2012). Thus, $\bullet\text{OH}$ was the active species in $\text{Bi}_2\text{O}_3\text{-ZNR}$ nanocomposites and finally induced the degradation of the EDCs. Moreover, $\text{Bi}_2\text{O}_3(1 \text{ at.}\%)\text{-ZNR}$ nanocomposites produced the more active $\bullet\text{OH}$ than other samples, with maximal photocatalytic activity, which also coincided with the results of photoluminescence emission spectra in Fig. 8a. Previous studies reported that active $\bullet\text{OH}$ can be observed with electron spin resonance technique for the catalysts in the dye oxidation process (Qiu et al. 2008; Zhang et al. 2009). The result in this study further provided the evidence of the $\bullet\text{OH}$ formation for $\text{Bi}_2\text{O}_3\text{-ZNR}$ nanocomposites under fluorescent light.

4 Conclusions

The $\text{Bi}_2\text{O}_3\text{-ZNR}$ nanocomposites with Bi_2O_3 nanoparticles incorporated with ZNRs have been obtained by combining hydrothermal technique with chemical-precipitation method. The structure, morphologies, and optical properties of the as-prepared nanocomposites were confirmed by XRD, FESEM, TEM, EDX, FTIR, UV-vis, and PL measurements. The investigation of photocatalytic ability showed that the $\text{Bi}_2\text{O}_3\text{-ZNR}$ nanocomposites exhibited higher photocatalytic activity than pure ZNRs for the degradation of both phenol and methylparaben under fluorescent light irradiation due to the enhancement of the separation of charge carriers between the Bi_2O_3 and the ZNRs. Probably, the strategy presented in this work would provide clues for developing new types of photocatalyst for practical applications in indoor environment.

Acknowledgments This research was supported by a Research Universiti grant (no. 814176) and a Post Graduate Research Grant Scheme (no. 8045030) from Universiti Sains Malaysia as well as a My PhD scholarship through the Malaysian Government.

References

- Benotti, M. J., Trenholm, R. A., Vanderford, B. J., Holady, J. C., Stanford, B. D., & Snyder, S. A. (2009). Pharmaceuticals and endocrine disrupting compounds in U.S. drinking water. *Environmental Science and Technology*, *43*, 597–603.
- Brouwers, M. M., Besselink, H., Bretveld, R. W., Anzion, R., Scheepers, P. T. J., Brouwer, A., et al. (2011). Estrogenic and androgenic activities in total plasma measured with reporter-gene bioassays: relevant exposure measures for endocrine disruptors in epidemiologic studies? *Environment International*, *37*, 557–564.
- Flores, N. M., Pal, U., & Mora, E. S. (2011). Photocatalytic behavior of ZnO and Pt-incorporated ZnO nanoparticles in phenol degradation. *Applied Catalysis A: General*, *394*, 269–275.
- Gultekin, I., & Ince, N. H. (2007). Synthetic endocrine disruptors in the environment and water remediation by advanced oxidation processes. *Journal of Environmental Management*, *85*, 816–832.
- Hameed, A., Gombac, V., Montini, T., Felisari, L., & Fornasiero, P. (2009). Photocatalytic activity of zinc modified Bi_2O_3 . *Chemical Physics Letters*, *483*, 254–261.
- Harvey, P. W., & Everett, D. J. (2004). Significance of the detection of esters of p-hydroxybenzoic acid (parabens) in human breast tumours. *Journal of Applied Toxicology*, *24*, 1–4.
- He, J., Luo, Q., Cai, Q. Z., Li, X. W., & Zhang, D. Q. (2011). Microstructure and photocatalytic properties of WO_3/TiO_2 composite films by plasma electrolytic oxidation. *Materials Chemistry and Physics*, *129*, 242–248.
- Huang, W. B., & Chen, C. Y. (2010). Photocatalytic degradation of diethyl phthalate (DEP) in water using TiO_2 . *Water, Air, and Soil Pollution*, *207*, 349–355.
- Ishibashi, K. I., Fujishima, A., Watanabe, T., & Hashimoto, K. (2000). Quantum yields of active oxidative species formed on TiO_2 photocatalyst. *Journal of Photochemistry and Photobiology A: Chemistry*, *134*, 139–142.
- Jia, T. K., Wang, W. M., Long, F., Fu, Z. Y., Wang, H., & Zhang, Q. J. (2009). Fabrication, characterization and photocatalytic activity of La-doped ZnO nanowires. *Journal of Alloys and Compounds*, *484*, 410–415.
- Kaneko, M., & Okura, I. (2002). *Photocatalysis science and technology* (pp. 261–276). New York: Springer.
- Kundu, V., Himan, R. L., Maan, A. S., & Goyal, D. R. (2009). Optical and spectroscopic studies of $\text{ZnO-Bi}_2\text{O}_3\text{-B}_2\text{O}_3$ glasses. *Journal Optoelectronics and Advanced Materials*, *11*, 1595–1600.
- Lam, S. M., Sin, J. C., & Mohamed, A. R. (2010). Parameter effect on photocatalytic degradation of phenol using $\text{TiO}_2\text{-P25/activated carbon (AC)}$. *Korean Journal of Chemical Engineering*, *27*, 1109–1116.
- Lam, S. M., Sin, J. C., Abdullah, A. Z., & Mohamed, A. R. (2012). Degradation of wastewaters containing organic

- dyes photocatalysed by zinc oxide: a review. *Desalination and Water Treatment*, 41, 131–169.
- Lam, S. M., Sin, J. C., Abdullah, A. Z., & Mohamed, A. R. (2013a). ZnO nanorod surface-decorated by WO₃ nanoparticles for photocatalytic degradation of endocrine disruptors under a compact fluorescent lamp. *Ceramics International*, 39, 2343–2352.
- Lam, S. M., Sin, J. C., Abdullah, A. Z., & Mohamed, A. R. (2013b). Green hydrothermal synthesis of ZnO nanotubes for photocatalytic degradation of methylparaben. *Materials Letters*, 93, 423–426.
- Lau, G. K., Zhang, T. S., & Goh, G. K. L. (2010). Photochemical properties of CeO₂-coated ZnO nanorods. *Journal of Nanoscience and Nanotechnology*, 10, 4733–4737.
- Liu, J. P., Huang, X. T., Li, Y. Y., Ji, X. X., Li, Z. K., He, X., et al. (2007). Vertically aligned 1D ZnO nanostructures on bulk alloy substrates: direct solution synthesis, photoluminescence and field emission. *Journal of Physical Chemistry C*, 111, 4990–4997.
- Liu, Z. Y., Bai, H. B., Xu, S. P., & Sun, D. D. L. (2011). Hierarchical CuO/ZnO “corn-like” architecture for photocatalytic hydrogen generation. *International Journal of Hydrogen Energy*, 36, 13473–13480.
- Liu, S. Z., Zhang, Y. C., Wang, T. X., & Yang, F. X. (2012). Green synthesis of hollow-nanostructured ZnO₂ and ZnO. *Materials Letters*, 71, 154–156.
- Mohajerani, M. S., Lak, A., & Simchi, A. (2009). Effect of morphology on the solar photocatalytic behavior of ZnO nanostructures. *Journal of Alloys and Compounds*, 485, 616–620.
- Nayak, J., Sahu, S. N., Kasuya, J., & Nozaki, S. (2008). CdS–ZnO composite nanorods: synthesis, characterization and application for photocatalytic degradation of 3,4-dihydroxy benzoic acid. *Applied Surface Science*, 254, 7215–7218.
- Pant, H. R., Park, C. H., Pant, B., Jing, L. D. T., Kim, H. Y., & Kim, C. S. (2011). Synthesis, characterization, and photocatalytic properties of ZnO nano-flower containing TiO₂ NPs. *Ceramics International*, 38, 2943–2950.
- Pardeshi, S. K., & Patil, A. B. (2008). A simple route for photocatalytic degradation of phenol in aqueous zinc oxide suspension using solar energy. *Solar Energy*, 82, 700–705.
- Park, W. I., Kim, D. W., Jung, S. W., & Yi, G. C. (2006). Catalyst-free growth of ZnO nanorods and their nanodevice applications. *International Journal of Nanotechnology*, 3, 373–395.
- Pugazhendhi, D., Pope, G. S., & Darbre, P. D. (2005). Oestrogenic activity of p-hydroxybenzoic acid (common metabolite of paraben esters) and methylparaben in human breast cancer cell lines. *Journal of Applied Toxicology*, 25, 301–309.
- Qiu, R. L., Zhang, D. D., Mo, Y. Q., Song, L., Brewer, E., Huang, X. F., et al. (2008). Photocatalytic activity of polymer-modified ZnO under visible light irradiation. *Journal of Hazardous Materials*, 156, 80–85.
- Qiu, Y. F., Yang, M. L., Fan, H. B., Zuo, Y. Z., Shao, Y. Y., Xu, Y. J., et al. (2011). Nanowires of α - and β -Bi₂O₃: phase-selective synthesis and application in photocatalysis. *Crystal Engineering Communications*, 13, 1843–1850.
- Sin, J. C., Lam, S. M., Mohamed, A. R., & Lee, K. T. (2012). Degrading endocrine disrupting chemicals from wastewater by TiO₂ photocatalysis: a review. *International Journal of Photoenergy*. doi:10.1155/2012/185159.
- Sin, J. C., Lam, S. M., Lee, K. T., & Mohamed, A. R. (2013). Preparation and photocatalytic properties of visible light-driven samarium-doped ZnO nanorods. *Ceramics International*. doi:10.1016/j.ceramint.2013.01.004.
- Sobczynski, A., Duczmal, L., & Zmudzinski, W. (2004). Phenol destruction by photocatalysis on TiO₂: an attempt to solve the reaction mechanism. *Journal of Molecular Catalysis A: Chemical*, 213, 225–230.
- Walker, C. H. (2009). *Organic pollutant: An ecotoxicological perspective* (pp. 265–292). Boca Raton: Taylor and Francis.
- Wang, Y. X., Li, X. Y., Lu, G., Chen, G. H., & Chen, Y. Y. (2008). Synthesis and photo-catalytic degradation property of nanostructured-ZnO with different morphology. *Materials Letters*, 62, 2359–2362.
- Wang, C. H., Shao, C. L., Wang, L. J., Zhang, L. N., Li, X. H., & Liu, Y. C. (2009a). Electrospinning preparation, characterization and photocatalytic properties of Bi₂O₃ nanofibers. *Journal of Colloid and Interface Sciences*, 333, 242–248.
- Wang, L. S., Xiao, M. W., Huang, X. J., & Wu, Y. D. (2009b). Synthesis, characterization, and photocatalytic activities of titanate nanotubes surface-decorated by zinc oxide nanoparticles. *Journal of Hazardous Materials*, 161, 49–54.
- Wang, X., Liu, G., Lu, G. Q., & Cheng, H. M. (2010). Stable photocatalytic hydrogen evolution from water over ZnO–CdS core-shell nanorods. *International Journal of Hydrogen Energy*, 35, 8199–8205.
- Wang, W., Lu, C. H., Ni, Y. R., Song, J. B., Su, M. X., & Xu, Z. Z. (2012). Enhanced visible-light photoactivity of 001 facets dominated TiO₂ nanosheets with even distributed bulk oxygen vacancy and Ti³⁺. *Catalysis Communications*, 22, 19–23.
- Yang, J. Y., Lin, Y., Meng, Y. M., & Liu, Y. H. (2012). A two-step route to synthesize highly oriented ZnO nanotube arrays. *Ceramics International*, 38, 4555–4559.
- Zhang, J., Sun, L. D., Liao, C. S., & Yan, C. H. (2002). A simple route towards tubular ZnO. *Chemical Communications*, 2002, 262–263.
- Zhang, X. Y., Dai, J. Y., Ong, H. C., Wang, N., Chan, H. L. W., & Choy, C. L. (2004). Hydrothermal synthesis of oriented ZnO nanobelts and their temperature dependent photoluminescence. *Chemical Physics Letters*, 393, 17–21.
- Zhang, L. S., Wang, W. Z., Yang, J., Chen, Z. G., Zhang, W. Q., Zhou, L., et al. (2006). Sonochemical synthesis of nanocrystallite Bi₂O₃ as a visible-light-driven photocatalyst. *Applied Catalysis A: General*, 308, 105–110.
- Zhang, J. H., Liu, H. Y., Wang, Z. L., & Ming, N. B. (2008). Low-temperature growth of ZnO with controllable shapes and band gaps. *Journal of Crystal Growth*, 310, 2848–2853.
- Zhang, D. D., Qiu, R. L., Song, L., Brewer, E., Mo, Y. Q., & Huang, X. F. (2009). Role of oxygen active species in the photocatalytic degradation of phenol using polymer sensitized TiO₂ under visible light irradiation. *Journal of Hazardous Materials*, 163, 843–847.